Resonance Raman Studies of Xanthine Oxidase: the Reduced Enzyme−Product Complex with Violapterin

Craig Hemann,[†] Predrag Ilich,[‡] Amy L. Stockert,[†] Eun-Young Choi,[†] and Russ Hille*,[†]

Department of Molecular and Cellular Biochemistry, The Ohio State University, Columbus, Ohio 43210, and Department of Chemistry & Biochemistry, Loras College, Dubuque, Iowa 52001

Received: July 28, 2004; In Final Form: October 26, 2004

A study of the molecular, electronic, and vibrational characteristics of the molybdenum-containing enzyme complex xanthine oxidase with violapterin has been carried out using density functional theory calculations and resonance Raman spectroscopy. The electronic structure calculations were carried out on a model consisting of the enzyme molybdopterin cofactor [in the four-valent, reduced state; Mo^{IV}O(SH)] covalently linked to violapterin (1*H*,3*H*,8*H*-pteridine-2,4,7-trione in the neutral form) via an oxygen bridge, Mo−O−C7. Full geometry optimizations were performed for all models using the SDD basis set and the three-parameter exchange functional of Becke combined with the Lee, Yang, and Parr correlational functional. Harmonic vibrational frequencies were determined for a variety of isotopes in an attempt to correlate experimentally observed shifts upon ^{18}O-labeling of the Mo−OR bridge to bound product as well as shifts seen upon substitution of solvent-exchangeable protons in samples prepared in D$_2$O. The theoretical vibrational frequencies compared favorably with experimentally observed vibrational modes in the resonance Raman spectra of the reduced xanthine oxidase−violapterin complex prepared in H$_2$O and D$_2$O and with ^{18}O-labeled product. Correlating the isotopic shifts from the calculations with those from the resonance Raman experiments resulted in complete normal mode assignments for all modes observed in the 350−1750 cm^{-1} range. The present work demonstrates that a model in which the violapterin is coordinated to the molybdenum of the active site in a simple end-on manner via the hydroxyl group introduced by an enzyme accurately predicts the observed resonance Raman spectrum of the complex. Given the numerous modes involving the bridging oxygen, a side-on binding mode can be eliminated.

Introduction

Xanthine oxidase (XO) or oxidoreductase catalyzes the final two steps of purine metabolism in eukaryotes by converting hypoxanthine to xanthine and xanthine to uric acid. The substrate specificity of this enzyme is very broad, ranging from simple aldehydes to pteridine derivatives such as lumazine [2,4(1*H*,3*H*)-pteridinedione]. As shown in Figure 1a, the active site for substrate oxidation has an LMo^{IV}O(SH) core in the reduced state, with L denoting 1 equiv of a pyranopterin cofactor coordinated to the molybdenum center via an enedithiolate side chain.[1,31] Characterization of the oxidized molybdenum center using X-ray absorption spectroscopy and X-ray crystallography has identified a molybdenum center with a distorted square-pyramidal geometry consisting of an oxo group (Mo=O, 1.68 Å), a Mo−OH group at 1.98 Å, and a bidentate enedithiolate ligand (equivalent Mo−S distances at 2.44 Å) defining the base of the pyramid with a sulfido group occupying the apical position (Mo=S, 2.15 Å). The reduced Mo^{IV} species has a similar five-coordinate geometry with an increase in the Mo−S bond length from 2.15 to 2.38 Å upon reduction, which has been attributed to protonation of the apical sulfido group.[2−5] By contrast, several theoretical studies have shown that the most stable conformer for this center has the oxo group in the apical position.[6−11] A magnetic circular dichroism study of the "very

rapid" Mo^V intermediate of XO generated using the slow substrate 2-hydroxy-6-methylpurine has indicated that the Mo=O bond is in the axial position oriented cis to the ene-1,2-dithiolate of the molybdenum cofactor. This contradiction with the crystal structure assignment has led to the suggestion that a conformational change may take place in the molybdenum coordination geometry during catalysis.[12] Very recently, a crystal structure of reduced xanthine oxidoreductase complexed with the inhibitor FYX-051 has been reported, in which the Mo=O group is found in the apical position.[39] Given the high level of specific activity exhibited by the enzyme used, the assignment is unambiguous, and it has been concluded that, in the earliest crystallographic studies, the positions of the molybdenum−oxo and −sulfido ligands have been misassigned.[32,34,36]

The presently available evidence supports a reaction mechanism for XO involving base-assisted nucleophilic attack by the Mo−OH group on the carbon to be hydroxylated (the C8 position in xanthine and the C7 position in lumazine), with a concomitant hydride transfer to the Mo=S group to yield a Mo^{IV}OR species.[1,13,14] The nature of the Mo−product complex has been investigated in an electron−nuclear double-resonance study of the "very rapid" species, again using 2-hydroxy-6-methylpurine as a substrate. This work has shown that the minimum distance from molybdenum to the C8 position of the bound product is 2.8 Å, consistent with simple end-on coordination of the product to the molybdenum center.[15] With lumazine as a substrate, the Mo^{IV} species that precedes the "very rapid" Mo^V intermediate in the catalytic sequence accumulates to a

* To whom correspondence should be sent. Phone: 614-292-3545. E-mail: hille.1@osu.edu.
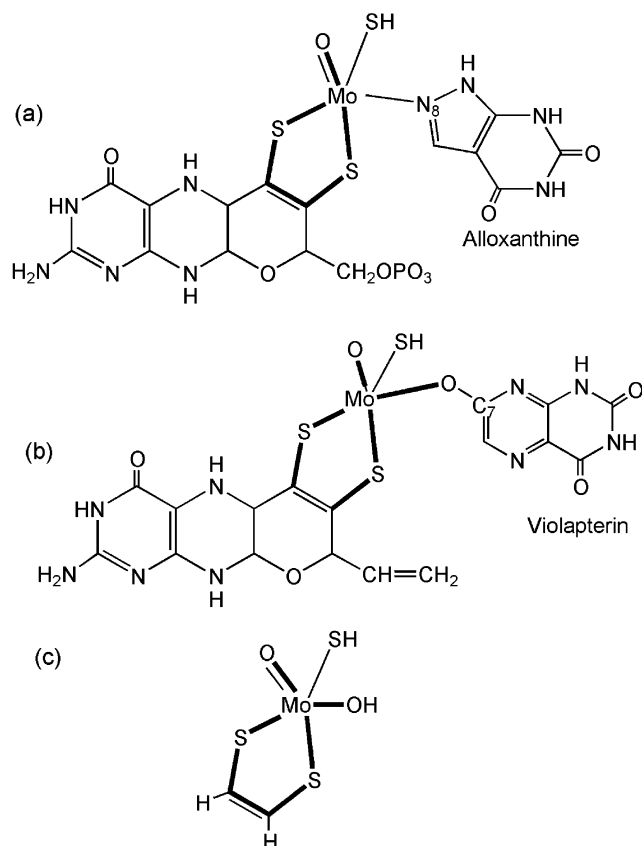† The Ohio State University.
‡ Loras College.

Figure 1. Schematic representation of the models considered in this study. (a) The XO molybdopterin cofactor–alloxanthine complex, PDB code 1JRP. (b) The enzyme–product XO/VO computational model used in this study. (c) Mo^{IV}–enedithiolate computational model of the enzyme cofactor.

significant degree in the course of the reaction and exhibits an absorption maximum at 650 nm. This E_{red}–P complex is an authentic catalytic intermediate in this reaction and can also be formed simply by the addition of violapterin to the dithionite-reduced enzyme; the 650 nm absorption has been assigned to a molybdenum-to-violapterin charge-transfer complex.[16,17] The bell-shaped pH dependence of k_{red}/K_d for the formation of this E_{red}–P complex from rapid reaction kinetic studies indicates that two ionizations are involved in forming this complex, with pK_a values of 6.4 and 7.8. The pK_a of 6.4 has been attributed to an active site glutamate (GLU1261; ref 36), and the pK_a of 7.8 has been assigned to the ionization of the N1 position of the pyrimidine ring of lumazine.[18,19]

A previous resonance Raman (rR) spectroscopic study of the E_{red}–P complex formed between reduced XO and violapterin used 676.4 nm excitation to enhance the Raman-active vibrational modes of the molybdenum-to-violapterin charge-transfer complex absorbing at 650 nm. A few empirical vibrational mode assignments were made by comparing the rR spectrum of the complex to a Raman spectrum of violapterin taken under the same experimental conditions, but no detailed normal mode assignments could be made at that time.[20]

In the present study, rR spectra for the E_{red}–violapterin charge-transfer complex excited at 647 nm have been analyzed with the aid of theoretical vibrational frequencies determined from density functional theory (DFT) calculations. Samples have been prepared in H_2O with both ^{16}O- and ^{18}O-labeled violapterin (the oxygen bound to the C7 position that coordinates to the reduced Mo^{IV} center in the charge-transfer complex) and in D_2O, providing a data set from which to correlate H/D isotopic mode

shifts of the bound violapterin and $^{16}O/^{18}O$ isotopic mode shifts of the Mo^{IV}–OR linkage. The theoretical model is of the $LMo^{IV}O(SH)P$ form, where L denotes a full pyranopterin–dithiolene truncated at the phosphate side chain and P denotes bound product (violapterin, in this case). Full molecular geometry optimizations and vibrational calculations for N/S-protonated, N/S-deuterated, and Mo^{IV}–^{18}OR-labeled models provide the basis for unambiguous normal mode assignments and correlation of vibrational mode shifts with isotopic substitution. Prior to exploring the model including the full pyrano-pterin–dithiolene and bound product, a much simpler $LMo^{IV}O$-(OH)(SH) model has been used to narrow the number of starting geometries in the large model calculations, where L is simply an enedithiolate ligand, Figure 1c.

Materials and Methods

Protein Purification. XO was purified from unpasteurized cow's milk using the purification procedure developed by Massey et al., with the following modification.[21] Elution of the hydroxylapatite column with a gradient from the dialysis buffer (0.1 M potassium phosphate, 0.3 mM EDTA, 1 mM salicylate, 10 μM PMSF, pH 6.0) to the elution buffer (0.1 M sodium pyrophosphate, 0.3 mM EDTA, pH 8.5) removed lactoperoxi-dase sufficiently to proceed directly to the S-200 column, bypassing the CM-52 column step. All fractions with an A_{276}/A_{450} ratio of less than 6.0 were pooled and concentrated. All enzyme preparations were 70–80% functional, as determined by methods described by Massey et al.[21]

Enzyme–Product Complex Sample Preparation. Each of the three rR samples was prepared with 70–80 μM XO in a 10 mM sodium pyrophosphate buffer (pH/D approximately 8.0). For each Raman sample, an approximate 2-fold stoichiometric excess of violapterin was added to the enzyme prior to making the system anaerobic. Exchanging the enzyme into D_2O involved running the concentrated enzyme through a small G-25 column swollen and equilibrated in 10 mM sodium pyrophosphate prepared in D_2O and adjusting the enzyme concentration as necessary. Preparation of the ^{18}O-labeled violapterin started with three 10-fold dilution/concentration steps with the enzyme in a buffer (approximately 500 μL total volume) prepared in $H_2^{18}O$ (Isotec, Inc.; 95% enrichment). Solid lumazine was added in small aliquots to approximately 500 μL of the enzyme solution and allowed to turn over. The conversion of lumazine to violapterin was monitored spectroscopically by spinning the system in a 3 kDa cutoff Centricon (Amicon, Inc.), removing a small volume of the filtrate, and comparing the UV/vis spectrum of the filtrate to those of lumazine and violapterin. The filtrate was added back to the enzyme pool until conversion to violapterin was complete. To generate the enzyme–violapterin charge-transfer complex for each of the three samples studied, approximately 1 mL of the enzyme/product mixture was placed in a tonometer and made anaerobic by cycling between a vacuum and an argon gas purge on an anaerobic train (approximately six cycles over a 45 min period). Approximately 5 mL of a separate buffer solution was placed in a test tube and bubbled with argon for approximately 15 min, solid dithionite was added, and the test tube was capped with a rubber septum. An anaerobic titration syringe was rinsed and filled with this dithionite solution and was then introduced to the sample tonometer through a rubber septum. Reduction was monitored in a standard UV/vis titration for complete bleaching of the 450 nm feature and maximal appearance of the 650 nm charge-transfer feature (see Figure 2 for representative UV/vis spectra). The sample was then removed from the tonometer using a 500
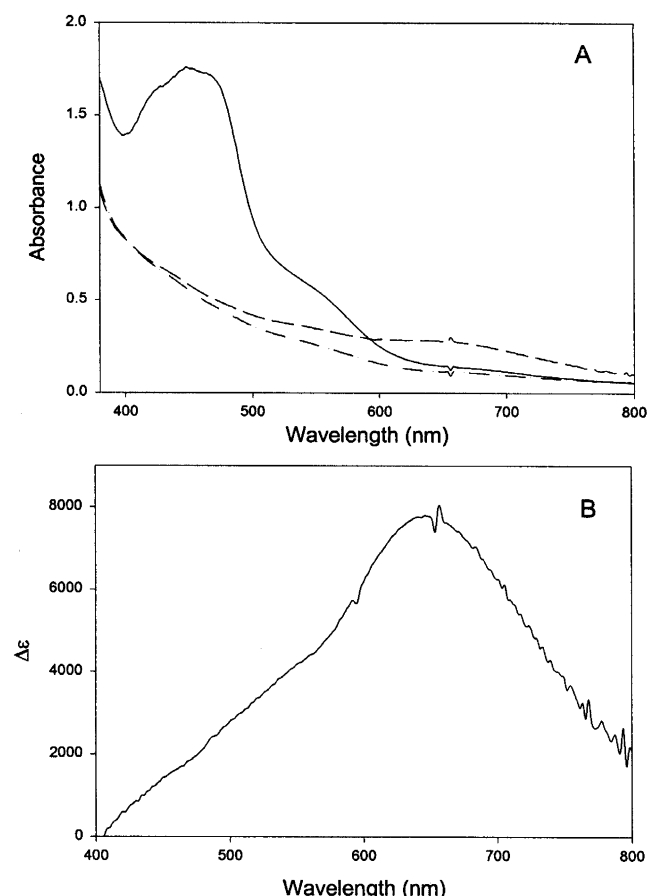
90 workstation and an Aspen Systems, Inc., Durango 500 alpha workstation, both running the OpenVMS operating system (Predrag Ilich, unpublished FORTRAN software).

Results and Discussion

A. Experiment. As shown in the visible absorption spectra of Figure 2, a long-wavelength absorption band is generated during the course of an anaerobic titration of oxidized XO with lumazine or an anaerobic titration of oxidized XO with dithionite in the presence of a slight stoichiometric excess of violapterin. Panel B of Figure 2 illustrates that this absorbance maximum occurs at approximately 650 nm, an ideal energy for excitation with the 647.1 nm line of a krypton gas laser in a rR spectroscopic study. As stated earlier, this complex is an authentic catalytic intermediate in the reaction of XO with lumazine, and the 650 nm absorption has been assigned to a molybdenum-to-violapterin charge-transfer complex.[16,17]

rR spectra recorded for this complex prepared in H_2O, H_2O with violapterin labeled with ^{18}O at the C7 position, and D_2O are shown in Figure 3. These samples have been prepared with the intact enzyme containing all redox-active sites, including molybdenum, two 2Fe/2S clusters of the spinach ferredoxin type, and one flavin adenine dinucleotide cofactor. Samples have also been prepared with the "deflavo" form of the enzyme, generating rR spectra identical to those shown in Figure 3 (data not shown) and demonstrating that the rR spectral features arise from the Mo^{IV}−violapterin charge-transfer complex.

A comparison of the lower spectrum (H_2O) with that of the middle spectrum (C7−^{18}O) shows that only five vibrational modes have shifted by 5 cm^{-1} or more (all downshifts) upon ^{18}O-labeling of the Mo−O−R linkage to the product. Two of these mode pairs are at a high enough frequency that there may be some C7=O stretching character in the modes: the Q25−Q26 pair at 1563 and 1548 cm^{-1}, corresponding to a shift of −15 cm^{-1}, and the Q30−Q31 mode pair at 1467 and 1455 cm^{-1}, corresponding to a shift of −12 cm^{-1}. The remaining three mode pairs (Q50−Q50, Q70−Q71, and Q75−Q75) occur at vibrational frequencies below 1200 cm^{-1} and may be composed of some displacement of the bridging oxygen coupled to more complex heterocycle motions. These mode pairs are much less affected by ^{18}O-labeling of the Mo−O−R linkage, displaying downshifts of only 5 cm^{-1} in each case.

Deuteration of the exchangeable sites in the complex has a much greater effect on the vibrational frequencies, reflected in the rR spectrum, than ^{18}O-labeling of the Mo−O−R linkage. A comparison of the top spectrum (D_2O) with the bottom spectrum (H_2O) illustrates several significant shifts. Large downshifts occur in the carbonyl stretching region, for example, Q17−Q18, −32 cm^{-1}; Q19−Q20, −57 cm^{-1}; and Q25−Q24, −27 cm^{-1}. Several of the bands at intermediate frequencies also display quite large shifts, making empirical vibrational band correlations quite difficult. For this reason, theoretical calculations were used to aid in the mode correlation, assignment, and details of individual vibrational mode composition.

B. The Models. The electronic structure calculations were done on two models of the XO molybdenum cofactor. In the first, Figure 1b, the initial geometry corresponded to the experimental structure of the alloxanthine-inhibited form of *Rhodobacter capsulatus* xanthine dehydrogenase reported by Kisker et al., shown in Figure 1a (PDB accession code of 1JRP)[31] with the following modifications: (i) the 2-carbophosphate group of the dihydropyrane ring was replaced with a vinyl group, (ii) the pyrazine moiety of the pterin ring was protonated, and (iii) the apical sulfo ligand on molybdenum was replaced

Figure 2. (A) Representative UV/vis spectra of oxidized XO (solid line), reduced XO (lower dashed line), and the reduced XO−violapterin complex (upper dashed line). (B) Difference spectrum of (reduced XO−violapterin complex)−(reduced XO).

μL long-needled, gastight Hamilton syringe that had been rinsed with anaerobic buffer, and it was injected through a rubber septum into an anaerobic quartz rR sample cell that had been previously purged with argon gas for at least 15 min. All rR spectra were collected from aqueous samples mounted in a Teflon sleeve and spun throughout the time of data collection in a standard NMR tube spinner.

Spectroscopy. The Raman instrument and software have been described previously.[19,22] All samples remained reduced throughout the time of rR data collection, as judged by UV/vis spectra taken directly after the rR experiments. Upon reoxidation or loss of the product-bound form of the enzyme, there would have been a very obvious color change due to a loss of the 650 nm absorption.

Calculation. Full molecular geometry optimizations, vibrational frequencies, and infrared intensities were obtained using the hybrid HF/DFT-B3LYP (HF = Hartree−Fock; B3LYP = the three-parameter exchange functional of Becke combined with the Lee, Yang, and Parr correlation functional) formalism[27,28] (referred to as DFT-B3LYP throughout) for four different models of the $LMo^{IV}O(SH)P$ center of XO. In each case, the full pyranopterin moiety was modeled with the four forms differing in the relative positions of the =O, −SH, and −P ligands (see Figure 5 for all four models). The SDD basis set was used for all calculations, and no reaction field was employed.[29] Calculations were performed using the Gaussian 98[30] program, running on a Silicon Graphics Octane2 computer controlled by the IRIX operating system. Further data analysis was performed on a Digital Equipment Corporation VAX 4000/
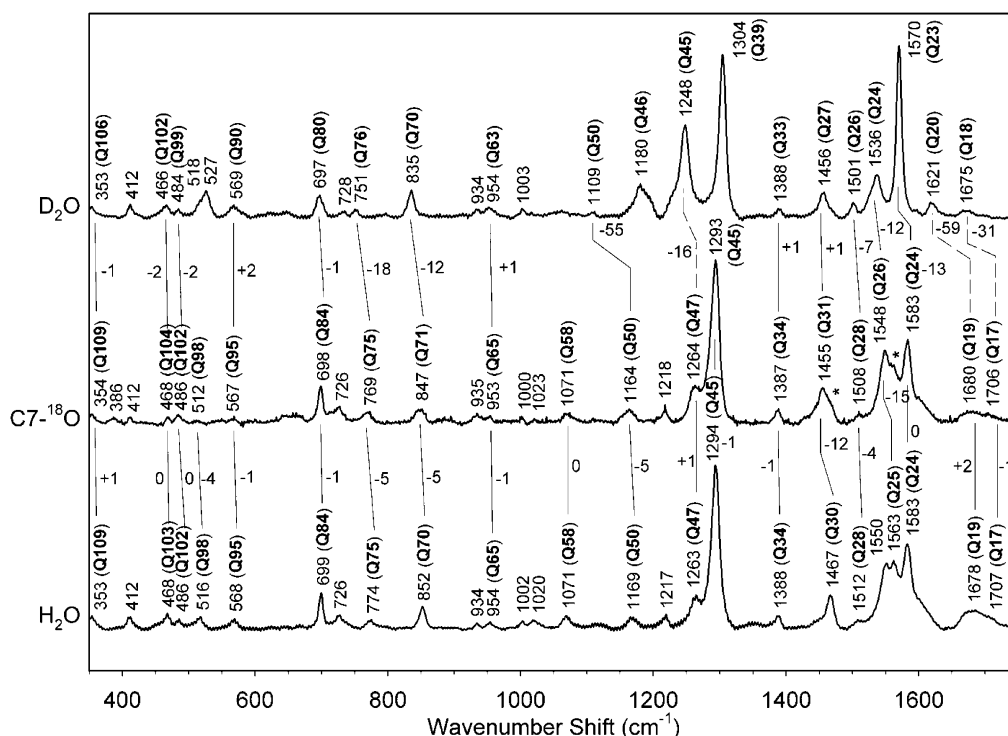
Figure 3. Correlation of the $^{16}O/^{18}O$ and H/D isotopic shifts for the experimental rR spectra for the N-protonated, ^{18}O-labeled, and N-deuterated forms of the Mo^{IV}–violapterin complex of XO. Strong mode correlations are shown as solid lines and approximate correlations as dashed lines. Each correlation line is labeled with the corresponding isotopic shift magnitude. All frequencies are in cm^{-1}. * denotes residual bands due to unlabeled violapterin.

by a sulfhydryl group. Finally, we replaced the alloxanthine substrate (from the Truglio et al. study[31]) with violapterin by connecting its C7 through an oxygen bridge to the two-electron-reduced molybdenum, Mo^{IV}, center. The second, "minimal" model consisted of the Mo–enedithiolate ring only, as shown in Figure 1c.

The geometry optimization calculations of the cofactor alone were carried out with the "large" cofactor model (51 atoms and 146 electrons; Figure 1b) and the "small" cofactor model (12 atoms and 48 electrons, consisting of a Mo–enedithiolate complex; Figure 1c). Using the DFT-B3LYP/SDD level of theory, the final optimized geometry for the "large" model of Figure 1b had the =O group in the apical position and the –SH group in the equatorial plane defined by this group, the oxygen from violapterin, and the two sulfur atoms of the enedithiolate. Although at odds with the existing protein crystal assignments, an optimized geometry in which the =O group assumed the apical position is consistent with results from many previous theoretical studies of models of the molybdenum center in various oxidation states and also with a variety of studies of simple Mo=O compounds.[6–11] With this unexpected result using the larger model, we decided to explore the much smaller model shown in Figure 1c, with the relative positions of the =O, –OH, and –SH ligands systematically varied in the starting geometries. In the "small" model study, we have found that, in all optimized geometries, the =O group has assumed the apical position. The energies for these fully optimized molecules are essentially isoenergetic (see, in the Supporting Information, Figure 1S for the "small" model results, Table 1S for final energies, and Tables 2S–7S for Cartesian coordinates of the final geometries for each of the six models shown in Figure 1S). The result of this "small" model survey indicated that there were four specific geometries to pursue in the "large" cofactor model.
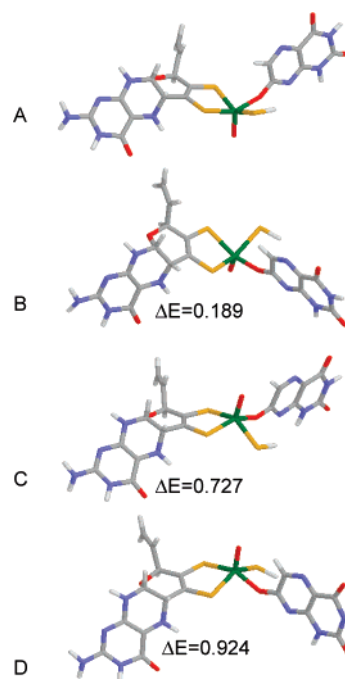

Figure 4. Four models of the reduced molybdenum center of XO complexed with violapterin used in this study. The energy differences relative to part A are shown. Energy differences are in units of kcal/mol. Atom coloring is Mo (green), S (yellow), O (red), C (gray), N (blue), and H (white). All illustrations were made using Molekel 4.0[37] and Rasmol V2.7.2.1.[38]

The four models calculated with the full pyranopterin cofactor and the violapterin ligand are shown in Figure 4A–D. These geometries have been fully optimized at the DFT-B3LYP/SDD level of theory and are ordered from the most stable (A) to the least stable (D), with the energy differences indicated.[33] Not
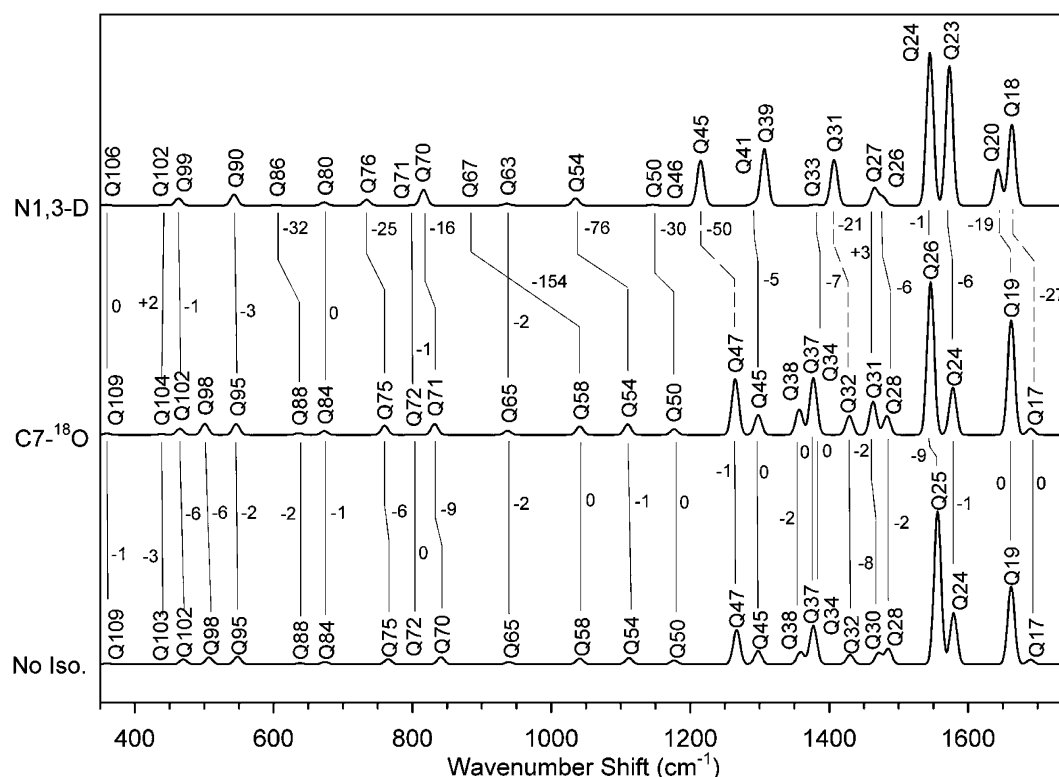
Resonance Raman Studies of Xanthine Oxidase

J. Phys. Chem. B, Vol. 109, No. 7, 2005 **3027**

Figure 5. Correlation of the $^{16}O/^{18}O$ and H/D isotopic shifts for the simulated Raman spectra for the N-protonated, ^{18}O-labeled, and N-deuterated forms of the Mo^{IV}−violapterin complex of XO. Strong mode correlations are shown as solid lines and approximate correlations as dashed lines. Each correlation line is labeled with the corresponding isotopic shift magnitude. All frequencies are in cm^{-1}.

only was the model in Figure 4A the most stable, but the geometry also agreed to the greatest extent with those reported for the crystal structures of the alloxanthine-inhibited form of xanthine dehydrogenase[32] and the hypothetical urate complex of aldehyde oxidoreductase[34] with regard to the orientation of the bound violapterin, with the exception of the swapped Mo= O and Mo−SH positions, as discussed above. This geometry has been used for the vibrational normal mode study to follow. Very recently, a crystal structure of bovine milk xanthine oxidoreductase in complex with a slow substrate, FYX-051, has been reported.[39] In this new structure, the Mo=O group is clearly identified as occupying the apical position of the molybdenum coordination sphere, and it appears that in earlier crystallographic work the positions of the Mo=O and Mo=S (or Mo−SH of the reduced enzyme) were swapped. The most recent study gives a molybdenum coordination geometry fully consistent with that seen in the present geometry-optimized calculations.

C. Theoretical versus Experimental Vibrational Frequencies. The reduced enzyme−violapterin (E_{red}−P) complex was prepared in H_2O and D_2O and with ^{18}O-labeled VO (VO = violapterin) in H_2O, and rR spectra were collected for each of these samples. Full geometry optimizations were attempted for the four models described in the previous section (see Figure 4A−D) at the DFT-B3LYP/SDD level of theory, with convergence requirements met in all but one model (see Figure 4C).[33] Vibrational frequencies and infrared intensities were calculated for the three models that converged, and Raman scattering intensities were calculated for the model of Figure 4A for use in Raman spectral simulations. As discussed above, the model of Figure 4A was used in the vibrational analysis because it was the most stable of the four models and because its overall geometry resembled crystal structures of analogous systems with bound inhibitors.[32,34,36,39] Theoretical H/D shifts were calculated

for this model by substituting deuterons for protons at all exchangeable sites in the model, and the Mo−^{16}OR oxygen was substituted with ^{18}O to obtain the theoretical isotopic shift for exchange of this bridging oxygen. A comparison of the theoretical vibrational frequencies using natural isotopes for the models that converged (parts A, B, and D of Figure 4) is given in Table 8S in the Supporting Information. Cartesian coordinates for the fully optimized geometry of the molecule in Figure 4A are compiled in Table 9S in the Supporting Information.

For each of the models shown in Figure 4, a total of 51 atoms resulted in 147 theoretical normal modes of vibration. Those modes with an appreciable violapterin in-plane vibrational component were correlated for the various isotopes used by direct comparison of the mode plots from the calculations (see Figure 2S in the Supporting Information for a correlation table in mode plot form). These theoretical vibrational frequencies were then compared to the experimental vibrational frequencies seen in the rR spectra of the XO/VO charge-transfer complex taken under the three experimental conditions mentioned earlier (Figure 3). The theoretical vibrational frequencies and Raman intensities were also used to generate the simulated Raman spectra shown in Figure 5.

C.1. Accuracy of the Calculations. A direct comparison between calculated and experimental frequencies for the protonated, Mo−^{18}OR-labeled, and deuterated systems in the 350− 1750 cm^{-1} energy region is shown in Table 1. For the protonated and Mo−^{18}OR systems, 26 modes are expected in this region based on calculations, but only 20 modes have been observed and assigned in the experimental spectra. For the protonated system, the unsigned differences between observed and calculated frequencies range from 1 cm^{-1} for mode Q34 to 30 cm^{-1} for mode Q58, with an average unsigned difference of 12.9 cm^{-1} for the 20 modes compared. For the ^{18}O-labeled system, the unsigned differences range from 0 cm^{-1} for Q34 to 30 cm^{-1}

TABLE 1: Comparison of the Calculated and Observed Vibrational Frequencies for the N-Protonated, ^{18}O-Labeled, and N-Deuterated Mo^{IV}−Violapterin Complex of XO^{a-f}

N1H/N3H				C7−^{18}O				N1D/N3D			
mode	calcd	obsvd	|O − C|	mode	calcd	obsvd	|O − C|	mode	calcd	obsvd	|O − C|
Q17	1690	1707	17	Q17	1690	1706	16	Q18	1663	1675	12
Q19	1661	1678	17	Q19	1661	1680	1 9	Q20	10642	1621	21
Q24	1579	1583	4	Q24	1578	1583	5	Q23	1572	1570	2
Q25	1555	1563	8	Q26	1546	1548	2	Q24	1545	1536	9
Q28	1485	1512	27	Q28	1483	1508	25	Q26	1477	1501	24
Q30	1470	1467	3	Q31	1462	1455	7	Q27	1465	1456	9
Q32	1430	N.O.		Q32	1428	N.O.		Q31	1407	N.O.	
Q34	1387	1388	1	Q34	1387	1387	0	Q33	1380	1388	8
Q37	1376	N.O.		Q37	1376	N.O.					
								Q39	1306	1304	2
Q38	1359	N.O.		Q38	1357	N.O.					
Q45	1298	1294	4	Q45	1298	1293	5	Q41	1293	N.O.	
Q47	1266	1263	3	Q47	1265	1264	1	Q45	1215	1248	33
Q50	1176	1169	7	Q50	1176	1164	12	Q50	1146	1109	37
								Q46	1177	1180	3
Q54	1111	N.O.		Q54	1110	N.O.		Q54	1034	N.O.	
Q58	1041	1071	30	Q58	1041	1071	30	Q67	887	N.O.	
Q65	939	954	15	Q65	937	953	16	Q63	935	954	18
Q70	840	852	12	Q71	831	847	16	Q70	815	835	19
Q72	801	N.O.		Q72	801	N.O.		Q71	800	N.O.	
Q75	765	774	9	Q75	759	769	10	Q76	734	751	17
Q84	674	699	25	Q84	673	698	25	Q80	673	697	24
Q88	638	N.O.		Q88	636	N.O.		Q86	604	N.O.	
Q95	548	568	20	Q95	546	567	21	Q90	543	569	26
Q98	507	516	9	Q98	501	512	11				
Q102	471	486	15	Q102	465	486	21	Q99	464	484	20
Q103	443	468	25	Q104	440	468	28	Q102	442	466	24
Q109	360	353	7	Q109	359	354	5	Q106	359	353	6
		avg	12.9			avg	13.8			avg	16.5
		|O − C|				|O − C|				|O − C|	

^{a} All calculations done in vacuo with no frequency scaling. ^{b} All frequencies are in cm^{-1}. ^{c} Isotopic shifts are correlated by reading across the table rows. ^{d} \|O − C\| denotes the absolute value of observed frequency − calculated frequency, and the average of the unsigned differences is shown at the bottom of each section. ^{e} N.O. denotes not observed. ^{f} All calculated frequencies refer to the model of Figure 4A.

for Q58, with an average unsigned difference of 13.8 cm^{-1}. For the deuterated system, 25 theoretical vibrational modes are expected in this energy range but only 19 modes have been assigned in the experimental spectrum. The unsigned frequency differences for this set range from 2 cm^{-1} for Q23 and Q39 to 37 cm^{-1} for Q50, with an average unsigned difference of 16.5 cm^{-1} for the set.

C.2. Isotopic Shifts. As indicated above, theoretical vibrational modes for the model system using natural abundance isotopes, Mo−OR ^{16}O/^{18}O substitution, and H/D substitution have been correlated by direct comparison of the mode plots. The same correlations have been attempted for the experimental vibrational modes for direct comparison with calculations of both the ^{16}O/^{18}O and H/D isotopic shifts. The theoretical vibrational mode correlations are depicted in mode plot form in Figure 2S in the Supporting Information for all modes expected in the experimental energy region. These correlations are listed in Table 2 with the calculated and observed isotopic shifts for both the ^{16}O/^{18}O and H/D substitutions.

C.2.1. ^{16}O/^{18}O Isotopic Shifts. On the basis of the experimentally and theoretically supported reaction mechanism, formation of a bridge between Mo-coordinated O(H) and the substrate carbon (C8 in xanthine and C7 in pterin substrates) is an essential step in the oxidative hydroxylation catalyzed by the XO class of molybdopterin enzymes. Accordingly, a modification of this bridge by, for example, ^{18}O isotopic replacement should provide direct insight regarding molecular events at the enzyme catalytic site. Predicted vibrational frequency shifts from the DFT calculations for ^{18}O substitution of the bridging oxygen to the bound product are relatively small in magnitude, the largest shifts being 9 cm^{-1} for mode pairs

Q25−Q26 and Q70−Q71. Of the 26 modes expected in the energy region of interest, only 6 are expected to shift by 6 cm^{-1} or more. The magnitudes of these shifts are summarized in the central region of Table 2, and a pictorial mode plot representation of the correlation of each of these modes is shown in the first two columns of Figure 2S in the Supporting Information. In the carbonyl stretching region, Q25 (1555 cm^{-1}) and Q30 (1470 cm^{-1}) are expected to have significant downshifts of 9 and 8 cm^{-1}, respectively. The Q25 mode is dominated by a C7=O stretching component coupled to both C6H and N1H bending motions. There is also some ring distortion of the violapterin heterocycle, especially in the N1C8a/N8C8a region. The predicted frequency shift corresponds quite closely to the 1563 cm^{-1} to 1548 cm^{-1} shift seen in the experimental data, a downshift of 15 cm^{-1}. The Q30 mode has some C7=O stretching character but primarily involves a large ring distortion of the heterocycle. This mode also has a large N1H bending component. The predicted vibrational energies and ^{18}O isotopic shift correspond very closely to the experimental band shift of 1467 cm^{-1} to 1455 cm^{-1}, a downshift of 12 cm^{-1}. In the intermediate energy region (900−1400 cm^{-1}), the predicted vibrational energy shifts with ^{18}O substitution are minimal (−2 cm^{-1} or less), which agrees well with the very modest experimental band shifts seen in this region. In the energy region below 900 cm^{-1}, four modes have predicted downshifts of 6 cm^{-1} or more: the Q70−Q71 shift of 9 cm^{-1}, the Q75−Q75 shift of 6 cm^{-1}, the Q98−Q98 shift of 6 cm^{-1}, and the Q102−Q102 shift of 6 cm^{-1}. As expected in these lower energy modes, each pair involves large ring distortions of the heterocycle, but in each case, the bridging oxygen is also displaced. The experimental spectral shifts parallel the predicted ones for the

Resonance Raman Studies of Xanthine Oxidase

J. Phys. Chem. B, Vol. 109, No. 7, 2005 **3029**

TABLE 2: Comparison of the Calculated and Observed $^{16}O/^{18}O$ and H/D Isotopic Shifts for the Vibrational Modes of the Mo^{IV}−Violapterin Complex of XO[a]

mode correlations			$\Delta(C7-^{18}O/C7-^{16}O)$		$\Delta(D-H)$	
N1H/N3H	C7−^{18}O	N1D/N3D	calcd	obsvd	calcd	obsvd
Q17	Q17	Q18	0	−1	−27	−32
Q19	Q19	Q20	0	+2	−19	−57
Q24	Q24	Q23	−1	0	−7	−13
Q25	Q26	Q24	−9	−15	−10	−27
Q28	Q28	Q26	−2	+4	−8	−11
Q30	Q31	Q27	−8	−12	−5	−11
Q32	Q32	Q31	−2	N.O.	−23	N.O.
Q34	Q34	Q33	0	−1	−7	0
Q37	Q37		0	N.O.		
Q38	Q38		−2	N.O.		
Q45	Q45	Q41	0	−1	−5	N.O.
Q47	Q47	Q45	−1	+1	−51	−15
Q50	Q50	Q50	0	−5	−30	−60
Q54	Q54	Q54	−1	N.O	−77	N.O.
Q58	Q58	Q67	0	0	−154	N.O.
Q65	Q65	Q63	−2	−1	−4	0
Q70	Q71	Q70	−9	−5	−25	−17
Q72	Q72	Q71	0	N.O.	−1	N.O.
Q75	Q75	Q76	−6	−5	−31	−23
Q84	Q84	Q80	−1	−1	−1	−2
Q88	Q88	Q86	−2	N.O.	−34	N.O.
Q95	Q95	Q90	−2	−1	−5	+1
Q98	Q98		−6	−4		
Q102	Q102	Q99	−6	0	−7	−2
Q103	Q104	Q102	−3	0	−1	−2
Ql09	Q109	Q106	−1	+1	−1	0

[a] All numbers in cm^{-1}.

most part, with a Q70−Q71 shift of −5 cm^{-1}, a Q75−Q75 shift of −5 cm^{-1}, and a Q98−Q98 shift of −4 cm^{-1}. The Q102−Q102 experimental band correlation, on the other hand, shows no shift with ^{18}O substitution.

Overall, the agreement between experimental rR band frequencies and ^{18}O isotopic shifts with calculations makes these five mode shifts a very reliable and specific indicator of ^{18}O-labeling of the Mo−OR bridge in the XO/VO charge-transfer complex.

C.2.2. H/D Isotopic Shifts. As seen in previous vibrational studies of lumazine and violapterin prepared in both H$_2$O and D$_2$O,[19,35] correlation of vibrational modes between protonated and deuterated species is made difficult because of changes in heterocycle mode composition upon deuteration, along with strong coupling of NH/ND bending motions shifting from the higher energy modes (1350 cm^{-1} and higher) for the protonated species to modes with energies below 1250 cm^{-1} upon deuteration. It is evident from the mode plots of the protonated model shown in Figure 2S (column 1) in the Supporting Information that nearly every mode has some amount of NH bending character and that this coupling is appreciable in all modes above 1350 cm^{-1} (Q17−Q38). For the deuterated model (Figure 2S, column 3), on the other hand, a weak ND bending component is apparent in only a few modes above 1300 cm^{-1}. Coupling to an ND bending component does become appreciable, however, in several modes below 1250 cm^{-1}, beginning with Q45 at 1215 cm^{-1}. Predicted H/D shifts range from −1 cm^{-1} to very substantial shifts for those mode pairs that maintain a large ND bending component upon deuteration: the Q54−Q54 pair has a predicted shift of −77 cm^{-1} and the Q58−Q67 pair one of −154 cm^{-1}. All 23 predicted mode shifts with deuteration in the energy range sampled by experiment are expected to be shifted to lower energy. These shifts are summarized in the last two columns of Table 2.

In the carbonyl stretching region (approximately 1500−1700 cm^{-1}), the highest energy vibrational mode in the protonated model (Q17) is predicted to be a C2=O stretching mode coupled to a strong N1H/N3H bend at 1690 cm^{-1}. In the deuterated model, the highest energy carbonyl mode (Q18) is best described as a coupled in-phase C2=O/C4=O stretch dominated by the C2=O stretching component at 1663 cm^{-1}, a predicted downshift of 27 cm^{-1}. In the experimental spectra, Q17 is assigned to the band observed at 1707 cm^{-1} in the rR spectrum of the sample prepared in H$_2$O and Q18 to that seen at 1675 cm^{-1} in the D$_2$O spectrum, an observed shift of −32 cm^{-1} that is in fair agreement with the calculated shift of −27 cm^{-1}. The Q19−Q20 pair is correlated because of the dominant C4=O stretching component coupled to an N3H(D) bending component. The Q19 mode has a predicted vibrational frequency of 1661 cm^{-1} in the protonated species that shifts to 1642 cm^{-1} (Q20) for the deuterated species, a theoretical H/D shift of −19 cm^{-1}. The experimental frequencies for the corresponding modes are 1678 and 1621 cm^{-1}, respectively, indicating a larger observed downshift of 57 cm^{-1}. The next four mode pairs (Q24−Q23, Q25−Q24, Q28−Q26, and Q30−Q27) all involve displacement of the C7 position of the bound violapterin and some C7−O stretching character mixed with both heterocycle distortions and NH/CH bending components for the protonated model. In the deuterated model, the majority of this normal mode character is maintained, except that the NH bending component is lost in all four cases. The largest predicted downshift is 10 cm^{-1} for the Q25−Q24 pair, which may be compared with the experimentally observed shift of −27 cm^{-1}. The other three pairs are predicted to have smaller shifts: for Q24−Q23, −7 cm^{-1}; for Q28−Q26, −8 cm^{-1}; and for Q30−Q27, −5 cm^{-1}. The experimental shifts for these mode pairs are −13, −11, and −11 cm^{-1}, respectively.

Of the remaining 11 mode pairs that have been assigned in the experimental data, four are predicted to have downshifts greater than 10 cm^{-1} upon deuteration: a −51 cm^{-1} shift of Q47−Q45, a −30 cm^{-1} shift of Q50−Q50, a −25 cm^{-1} shift of Q70−Q70, and a −31 cm^{-1} shift of Q75−Q76. Each of these modes maintains a substantial ND bending component in the deuterated form (although the mode correlation for the Q47−Q45 pair is somewhat weaker than those for the other mode pairs). The observed H/D shifts for these mode pairs are −15, −60, −17, and −23 cm^{-1}, respectively.

It is evident from the above discussion that the experimental vibrational frequency shifts with deuteration agree, in general, with the prediction that all deuterium shifts are downshifts in the energy region observed, although the magnitudes of specific shifts are quite different in some cases. For mode pairs Q19−Q20, Q25−Q24, and Q50−Q50, the observed deuterium shifts are much larger than predicted, and for mode pairs Q47−Q45, Q70−Q70, and Q75−Q76, the observed shifts are less than predicted. These discrepancies may reflect the inability to model the numerous specific protein interactions with the bound product (and, to a lesser extent, the pyranopterin cofactor). From the crystal structure of alloxanthine-inhibited xanthine dehydrogenase from *R. capsulatus*, the inhibitor interacts with several protein residues, including glutamic acid (E232 and E730), an arginine (R310), and a water molecule, with phenylalanines on each side of the inhibitor molecule (F344 and F459).[32] Another 14 hydrogen-bonding interactions between the polypeptide and pyranopterin cofactor are observed. Given the difficulties of modeling such interactions, the overall agreement between the calculated and observed shifts must be considered quite good.
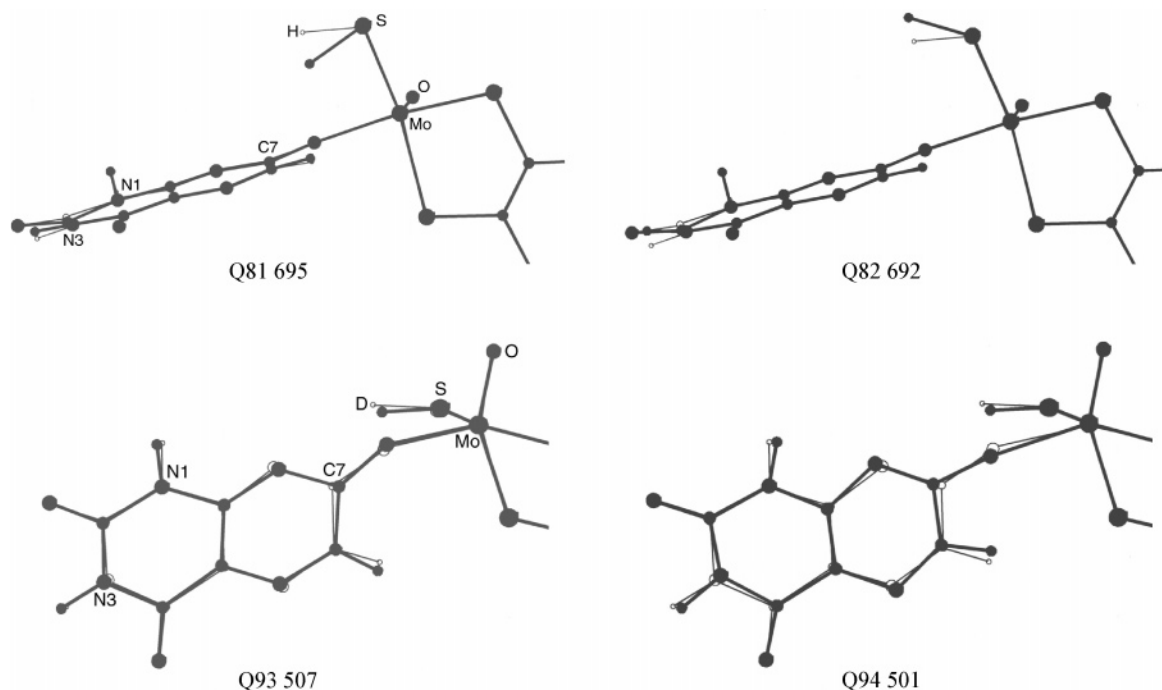
Figure 6. Mode plots of the SH bending modes Q81 and Q82 predicted by calculations to shift to modes Q93 and Q94 upon deuteration of sulfur. Notice in modes Q93 and Q94 that the SD bending component is coupled to violapterin in-plane modes that include displacement of the Mo^{IV}OR bridge. These vibrations are observed as an unresolved peak in the experimental D$_2$O data, fit best with two Gaussians centered at 518 (Q94) and 527 cm^{-1} (Q93). All mode plot frequencies are in cm^{-1}.

C.2.3. Sulfhydryl Bending Modes. An interesting observation in the experimental rR data shown in Figure 3 is that there is a fairly intense feature in the D$_2$O spectrum in the 520 cm^{-1} region. This is the most intense feature in all experimental spectra below 650 cm^{-1} and is fit best by two Gaussians centered at 518 and 527 cm^{-1}. The theoretical vibrational frequency calculations for each of the isotopes lend some insight into the normal mode assignments for these spectral features. The calculations suggest that there are two modes in the protonated and ^{18}O-labeled models that are dominated by an SH bending component: Q81 at 695 cm^{-1} and Q82 at 692 cm^{-1}. These SH bending components are in the equatorial plane of the molybdenum coordination sphere (see the mode plots of Figure 6 for complete details) and are coupled to out-of-plane bending motions of the NH groups of the bound violapterin in both cases. It is evident from the experimental rR spectra of the samples prepared in H$_2$O and in H$_2$O with ^{18}O-labeled product that there are no obvious spectral features between modes Q95 and Q84 (570−695 cm^{-1}), suggesting that these SH bending modes have weak Raman scattering intensities and are not resonance-enhanced with laser excitation at 647.1 nm. Calculated vibrational frequencies for the deuterated model suggest that the SH bends shift to much lower frequencies with deuteration and couple to low-energy in-plane violapterin heterocycle modes. These modes are Q93 (predicted at 507 cm^{-1}) and Q94 (predicted at 501 cm^{-1}). As shown in Figure 6, both of these modes involve some distortion of the pyrazine moiety of violapterin and some displacement of the oxygen bridge to the molybdenum center, perhaps resulting in resonance enhancement upon excitation within the absorption envelope of the charge-transfer complex. The experimental vibrational frequencies of 527 and 518 cm^{-1} are in reasonable agreement with the calculated frequencies for these modes.

Conclusions

We have collected, calculated, and assigned vibrational spectra of the reduced enzyme−violapterin complex of XO. The experimental data were collected using rR spectroscopy with excitation in the absorption envelope of the charge-transfer complex formed between the fully reduced enzyme and violapterin. The enzyme−product samples were prepared in H$_2$O and D$_2$O and also with the ^{18}O-isotope congener as well as the ^{16}O-containing form. The experimental vibrational bands were assigned with the aid of DFT calculations carried out for a series of conformers and isotopic variants of a model for the active site possessing a more realistic representation of the pterin cofactor in an LMo^{IV}O(SH) configuration with a bridging oxygen to violapterin (Figure 1B). The calculations were performed using the B3LYP exchange-correlation functional[27,28] with the SDD basis set.[29] A direct comparison of the calculated vibrational frequencies with those of the experiment for each sampling condition and a correlation of isotopic shifts have led to complete vibrational mode assignments for the rR spectra of all of the samples studied in the 350−1750 cm^{-1} energy region.

Vibrational frequencies resulting from the DFT-B3LYP/SDD method calculations, done in vacuo with no frequency scaling, simulate the experimental data closely for each isotope studied. The average unsigned errors are 12.9 cm^{-1} for the protonated system, 13.8 cm^{-1} for the ^{18}O-labeled system, and 16.5 cm^{-1} for the deuterated system; simple frequency scaling methods did not lessen these errors. In general, agreement between calculated and observed isotopic shifts is also good, especially for the substitution of ^{18}O for ^{16}O in the bridging position. Of the six modes predicted to shift by 6 cm^{-1} or more, five of these mode shifts are observed and assigned in the rR spectra, providing a useful spectroscopic handle for ^{18}O-labeling of the complex.

Resonance Raman Studies of Xanthine Oxidase

J. Phys. Chem. B, Vol. 109, No. 7, 2005 **3031**

The H/D isotopic shifts are much more complex by comparison, and the absolute magnitudes of the calculated and observed shifts do not agree in all cases (although the direction of shift does agree for all significant H/D shifts). The absolute accuracy of the calculated vibrational frequencies with those of the experiment could, in principle, be improved by including explicit interactions with protein residues anticipated to interact with bound violapterin from empirical observation of known crystal structures of analogous systems.[31,34,36,39] At present, however, it is not possible to model such interactions in a meaningful way with a realistic number of atoms. Experimentally, site-directed mutagenesis provides a tool for affecting specific protein interactions to bound products/substrates/ inhibitors. These specific interactions are expected to perturb the vibrational modes of bound violapterin, providing important information regarding the stabilization of the bound product. Details of these interactions could be elaborated by a comparison with the normal mode assignments made in this study.

In conclusion, we have undertaken a normal mode analysis that has led to specific assignments of vibrational modes seen in the rR spectra of the complex of reduced XO with product violapterin. The model used has simple end-on binding of the product to the active site molybdenum via the oxygen introduced by enzyme hydroxylation of substrate and provides a generally very accurate picture of the vibrational energies for each mode.

Supporting Information Available: Figure 1S details six "small" models showing the starting and fully optimized geometries. Table 1S contains the energies for the optimized geometries of the six models shown in Figure 1S. Tables 2S− 7S list the Cartesian coordinates for each of these optimized models. Table 8S compares the assigned vibrational frequencies of all fully optimized geometries of the molecules shown in Figure 4 of the main text. Table 9S lists the Cartesian coordinates of the model shown in Figure 4A of the main text, which is used for all vibrational assignments in this study. Table 10S compares the single-point energies of the model system of Figure 4A of the main text with successive 30° clockwise rotations of the bound violapterin about its C7−O bond. Figure 2S is a correlation table of the theoretical vibrational modes for each congener in mode plot form.

References and Notes

(1) Hille, R. *Chem. Rev.* **1996**, *96*, 2757−2816.

(2) Tullius, T. D.; Kurtz, D. M., Jr.; Conradson, S. D.; Hodgson, K. O. *J. Am. Chem. Soc.* **1979**, *101*, 2776−2779.

(3) Bordas, J.; Bray, R. C.; Garner, C. D.; Gutteridge, S.; Hasnain, S. S. *Biochem. J.* **1980**, *191*, 499−508.

(4) Cramer, S. P.; Wahl, R.; Rajagopalan, K. V. *J. Am. Chem. Soc.* **1981**, *103*, 7721−7727.

(5) Cramer, S. P.; Hille, R. *J. Am. Chem. Soc.* **1985**, *107*, 8164−8169.

(6) Bray, M. R.; Deeth, R. J. *Inorg. Chem.* **1996**, *35*, 5720−5724.

(7) Bray, M. R.; Deeth, R. J. *J. Chem. Soc., Dalton Trans.* **1997**, 1267.

(8) Voityuk, A. A.; Albert, K.; Köstlmeier, S.; Nasluzov, V. A.; Neyman, K. M.; Hof, P.; Huber, R.; Romão, M. J. *J. Am. Chem. Soc.* **1997**, *119*, 3159−3160.

(9) Voityuk, A. A.; Albert, K.; Romão, M. J.; Huber, R.; Rösch, N. *Inorg. Chem.* **1998**, *37*, 176−180.

(10) Ilich, P.; Hille, R. *J. Phys. Chem. B* **1999**, *103*, 5406−5412.

(11) Ilich, P.; Hille, R. *J. Am. Chem. Soc.* **2002**, *124*, 6796−6797.

(12) Jones, R. M.; Inscore, F. E.; Hille, R.; Kirk, M. L. *Inorg. Chem.* **1999**, *38*, 4963−4970.

(13) Xia, M.; Dempski, R.; Hille, R. *J. Biol. Chem.* **1999**, *274*, 3323− 3330.

(14) McWhirter, R. B.; Hille, R. *J. Biol. Chem.* **1991**, *266*, 23724− 23731.

(15) Manikandan, P.; Choi, E.-Y.; Hille, R.; Hoffman, B. M. *J. Am. Chem. Soc.* **2001**, *123*, 2658−2663.

(16) Davis, M. D.; Olson, J. S.; Palmer, G. *J. Biol. Chem.* **1982**, *257*, 14730−14737.

(17) Davis, M. D.; Olson, J. S.; Palmer, G. *J. Biol. Chem.* **1984**, *259*, 3526−3533.

(18) Kim, J. H.; Ryan, M. G.; Knaut, H.; Hille, R. *J. Biol. Chem.* **1996**, *271*, 6771−6780.

(19) Hemann, C.; Ilich, P.; Hille, R. *J. Phys. Chem. B* **2003**, *107*, 2139− 2155.

(20) Oertling, W. A.; Hille, R. *J. Biol. Chem.* **1990**, *265*, 17446−17450.

(21) Massey, V.; Brumby, P. E.; Komai, H.; Palmer, G. *J. Biol. Chem.* **1969**, *244*, 1682−1691.

(22) Ilich, P.; Hemann, C. F.; Hille, R. *J. Phys. Chem. B* **1997**, *101*, 10923−10938.

(23) Kohn, W.; Becke, A. D.; Parr, R. G. *J. Phys. Chem.* **1996**, *100*, 12974.

(24) Andzelm, J.; Wimmer, E. *J. Phys. Chem.* **1992**, *96*, 1280.

(25) Johnson, B. G.; Gill, P. M. W.; Pople, J. A. *J. Phys. Chem.* **1993**, *98*, 5612.

(26) Becke, A. D. *J. Chem. Phys.* **1993**, *98*, 5648.

(27) Becke, A. D. *Phys. Rev. A: At., Mol., Opt. Phys.* **1988**, *38*, 3098.

(28) Lee, C.; Yang, W.; Parr, R. G. *Phys. Rev. B: Condens. Matter* **1988**, *37*, 785.

(29) The SDD basis set uses the Stuttgart/Dresden effective core potential basis for all but first-row atoms and the Dunning/Huzinaga valence double-ζ basis (D95V) for first-row atoms. (a) Dunning, T. H., Jr.; Hay, P. J. In *Modern Theoretical Chemistry*; Schaefer, E. H., III, Ed.; Plenum: New York, 1976; pp 1−28. (b) Frisch, A. E.; Frisch, M. J. In *Gaussian 98 User's Reference*; Gaussian, Inc.: Pittsburgh, PA, 1994−1999.

(30) Frisch, M. J.; Trucks, G. W.; Schlegel, H. B.; Scuseria, G. E.; Robb, M. A.; Cheeseman, J. R.; Zakrzewski, V. G.; Montgomery, J. A., Jr.; Stratmann, R. E.; Burant, J. C.; Dapprich, S.; Millam, J. M.; Daniels, A. D.; Kudin, K. N.; Strain, M. C.; Farkas, O.; Tomasi, J.; Barone, V.; Cossi, M.; Cammi, R.; Mennucci, B.; Pomelli, C.; Adamo, C.; Clifford, S.; Ochterski, J.; Petersson, G. A.; Ayala, P. Y.; Cui, Q.; Morokuma, K.; Rega, N.; Salvador, P.; Dannenberg, J. J.; Malick, D. K.; Rabuck, A. D.; Raghavachari, K.; Foresman, J. B.; Cioslowski, J.; Ortiz, J. V.; Baboul, A. G.; Stefanov, B. B.; Liu, G.; Liashenko, A.; Piskorz, P.; Komaromi, I.; Gomperts, R.; Martin, R. L.; Fox, D. J.; Keith, T.; Al-Laham, M. A.; Peng, C. Y.; Nanayakkara, A.; Challcombe, M.; Gill, P. M. W.; Johnson, B.; Chen, W.; Wong, M. W.; Andres, J. L.; Gonzalez, C.; Head-Gordon, M.; Replogle, E. S.; Pople, J. A. *Gaussian 98*, revision A11.3; Gaussian, Inc.: Pittsburgh, PA, 2002.

(31) Truglio, J. J.; Theis, K.; Leimkühler, S.; Rappa, R.; Rajagopalan, K. V.; Kisker, C. *Structure* **2002**, *10*, 115−125.

(32) Amaya, Y.; Yamazaki, K.; Sato, M.; Noda, K.; Nishino, T.; Nishino, T. *J. Biol. Chem.* **1990**, *265*, 14170−14175.

(33) The model of Figure 4C reached convergence in only three of the four convergence criteria required for full geometry optimization in Gaussian 98.

(34) Huber, R.; Hof, P.; Duarte, R. O.; Moura, J. J. G.; Moura, I.; Liu, M.-Y.; LeGall, J.; Hille, R.; Archer, M.; Ramão, M. J. *Proc. Natl. Acad. Sci. U.S.A.* **1996**, *93*, 8846−8851.

(35) Michaud, A. L.; Herrick, J. A.; Duplain, J. E.; Manson, J. L.; Hemann, C.; Ilich, P.; Donohoe, R. J.; Hille, R.; Oertling, W. A. *Biospectroscopy* **1998**, *4*, 235−256.

(36) Enroth, C.; Eger, B. T.; Okamoto, K.; Nishino, T.; Nishino, T.; Pai, E. F. *Proc. Natl. Acad. Sci. U.S.A.* **2000**, *97*, 10723−10728.

(37) Flükiger, P.; Lüthi, H. P.; Portmann, S.; Weber, J. *Molekel 4.0*; Swiss Center for Scientific Computing: Manno, Switzerland, 2000.

(38) Sayle, R.; Mueller, A.; Grossman, G.; Molinaro, M.; Bernstein, H. *Rasmol*, V2.7.2.1, 1992−2001.

(39) Okamoto, K.; Matsumoto, K.; Hille, R.; Eger, B. T.; Pai, E. F.; Nishino, T. *Proc. Natl. Acad. Sci. U.S.A.* **2004**, *101*, 7931−7936.